



HAL
open science

Implementation and Comparison of Contact Models within PIRAT for Nuclear Reactivity Control Systems

Matthew Bonney, Maxime Zabiégo

► **To cite this version:**

Matthew Bonney, Maxime Zabiégo. Implementation and Comparison of Contact Models within PIRAT for Nuclear Reactivity Control Systems. *Journal of Vibration and Acoustics*, 2020, 142 (5), pp.051104. 10.1115/1.4046955 . cea-02558352

HAL Id: cea-02558352

<https://cea.hal.science/cea-02558352>

Submitted on 29 Apr 2020

HAL is a multi-disciplinary open access archive for the deposit and dissemination of scientific research documents, whether they are published or not. The documents may come from teaching and research institutions in France or abroad, or from public or private research centers.

L'archive ouverte pluridisciplinaire **HAL**, est destinée au dépôt et à la diffusion de documents scientifiques de niveau recherche, publiés ou non, émanant des établissements d'enseignement et de recherche français ou étrangers, des laboratoires publics ou privés.

Implementation and Comparison of Contact Models within PIRAT for Nuclear Reactivity Control Systems

Matthew S. Bonney, Maxime Zabiégo*

CEA Cadarache
CEA/DEN/CAD/DEC/SESC/LECIM
13108 St. Paul lez Durance, France

ABSTRACT

The Reactivity Control System is a vital safety system for a nuclear reactor. One of the most challenging aspects in the design of these systems is the operation during critical situations, in particular during earthquakes to safely shutdown the reactor. To study these situations, the toolbox PIRAT is used to model two types of excitation: stepped-sine and realistic. The main focus of this work is the comparison of the implementation of the contact models used to describe the interaction between the subsystems. For the dynamic tool in PIRAT (DEBSE), this is done with a two-stage linear spring or a Lankarani & Nikravesh based models. For the sine excitation, the results show four distinct response types with the maximum displacement varying between the models. Low frequency excitation showed little variance while higher frequency excitation showed large variations. The realistic excitation however, did not show these variations and showed nearly identical results for the contact models tested. This gives confidence in the simulations since the user selected contact model did not greatly affect the simulation results for a realistic excitation.

Nomenclature

RCS Reactivity Control System
FR Fast Reactor
MP Mobile Part
LS Lower Sleeve
US Upper Sleeve
CR Control Rod
DM Drive Mechanism
BCS Below Core Structure
ACS Above Core Structure
MSC Model System Configuration
PIRAT Python Implementation for Reliability Assessment Tools
StaBI Static Bresse Implementation
DEBSE Dynamic Euler-Bernoulli for Seismic Events
SIKI Step-by-step Kinetic Implementation
LG Lower Guide
IG Intermediate Guide
UG Upper Guide
FRF Frequency Response Function
BC Boundary Conditions
L&N Lankarani and Nikravesh
DAF Dynamic Amplification Factor

*Corresponding Author: maxime.zabiego@cea.fr

1 Introduction

For the operation of a nuclear reactor, the Reactivity Control System (RCS) is vital. The RCS has two main functions, to control the output of the reactor and to ensure safe shutdown operations during normal and abnormal situations. One of the most challenging abnormal situations to design around is excitation caused by seismic activity. This excitation may exhibit large displacements at low frequencies lasting for long periods of time.

This work specifically addresses the RCS dynamic behavior for Fast Reactors (FRs), although some of its content also applies to other types of reactors. This topic has long been of interest for FR development, through both experimental and numerical studies [1–10]. For FRs, a RCS is typically comprised of three main components:

- * A Mobile Part (MP), associated with the Control Rod (CR) that contains neutron absorbing material and its Drive Mechanism (DM). The MP retracts during full operation and inserts into the fissile core during shutdown operations, as seen in Fig. 1.
- * Two sleeves, which guide the MP during its vertical displacements:
 - * The Lower Sleeve (LS) guides the CR, and lies on top of the Below Core Structure (BCS) within a tightly packed lattice of the fuel sub-assemblies.
 - * The Upper Sleeve (US), which guides the DM, suspends from the Above Core Structure (ACS) and has relatively free lateral motion.

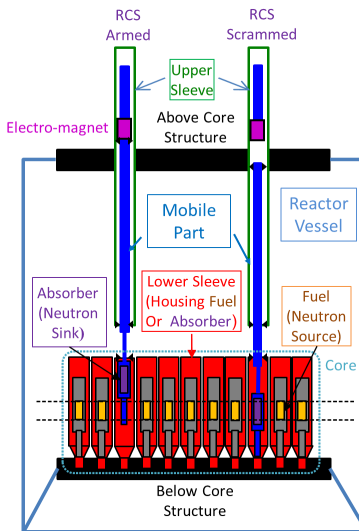


Fig. 1: Example motion of a RCS during operation

Ideally, the LS and US are well-aligned in order to guide the MP in its vertical motion. However, in practice, misalignments due to the deformation of the reactor structures exist, causing an increase in interactions with the MP. These extra interactions create friction and shear forces that act on the MP, possibly delaying the achievement of a safe shutdown. The misalignments come from many sources, of which some are dynamic and some static. These sources include, installation tolerance, dynamic excitation, irradiation bending, and tilt relative to vertical position to name a few. Modeling these deformations, including the dynamic seismic excitation, is difficult due to the complex characteristics. For the sake of simplicity, the analysis is restricted to the horizontal component of the deformations, with the assumptions that:

- * The ground excitation is transmitted to both the ACS and BCS through the reactor vessel structures.
- * The horizontal excitation of the BCS produces collective bending motions of the core fuel sub-assemblies that impose displacements to the rigid LS, which imposes displacements to the MP, primarily through the MP/LS contact at the top of the LS.
- * The horizontal excitation of the ACS (typically an order of magnitude lesser than that of the BCS) produces bending motions of the semi-rigid US, but the response of the MP/US interaction is primarily controlled by the motion of the MP caused by the LS-imposed horizontal displacements. For this study, the ACS excitation is neglected.

In order to address this issue during the design phase of a RCS, the Python Implementation for Reliability Assessment Tools (PIRAT), a novel computational tool package, is currently in development with three main tools:

- * StaBI (Static Bresse Implementation): A static tool based on the analytic representation of the Bresse formulations [11,12].
- * DEBSE (Dynamic Euler-Bernoulli for Seismic Events): A dynamic tool based on the analytic solution of the dynamic Euler-Bernoulli equation [13–15]. This tool is the main focus of this work.
- * SIKI (Step-by-step Kinetic Implementation): A kinetic tool based on iterations for either StaBI or DEBSE. This tool is currently in development to assess the MP drop time and the resulting delay in achieving a safe shutdown.

This work is organized as follows: Section 1.1 describes the example system used in this work. This system is not related to any current development reactor to better explain the details of the system. Section 2 gives the theory of the modeling used in DEBSE with a focus in Section 2.1 for the various contact models implemented. The theory used for StaBI is not presented in this work, but is documented fully in [12]. Simulation results for a stepped-sine excitation are in Section 3, while a more realistic excitation is explored in Section 4. Section 5 gives some concluding remarks about the findings in this work.

1.1 Model System

The model system used in this work is the Model System Configuration (MSC). This system is also used in [14, 15] to evaluate the development of DEBSE. The MSC system is similar to RCSs in various FRs, such as: ASTRID RBC [3], the Superphenix SCP [1], the Phenix BdC [16], or the PFBR CSR and CSRDM [5], but does not contain the proprietary data associated with those designs. The properties of the MSC system are:

- * The undeformed geometry (outer envelope of MP and inner envelope of the sleeves) are in Fig. 2a with the material properties (linear mass density and area moment of inertia) in Fig. 2b.
- * There are three nominal guide regions visualized in Fig. 2a. These are: the Lower Guide (LG) that is the bottom end of the MP and produces a sliding contact during operation, the Intermediate Guide (IG) that is the main excitation location, and the Upper Guide (UG) that is the main location of interaction between the MP/US and is the major response point.
- * The modal information via the Frequency Response Function (FRF) for the MP is in Fig. 3 with the first three associated mode shapes (showing the IG and UG levels for the intermediate stroke value used in this work).

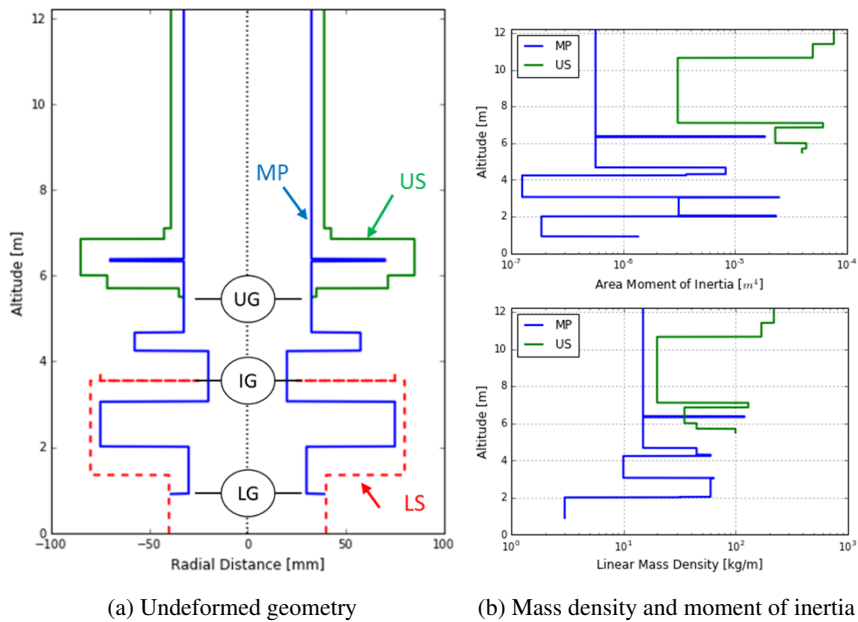


Fig. 2: Geometry and material properties of the MSC system

2 DEBSE Theory

To better explain this solver, Fig. 4 shows a simplified MP with two contact locations, x_k for a contact with the LS and x_m for a contact with the US. While Fig. 4 shows only one contact per sleeve, this analysis is valid for any number of contacts for either sleeve.

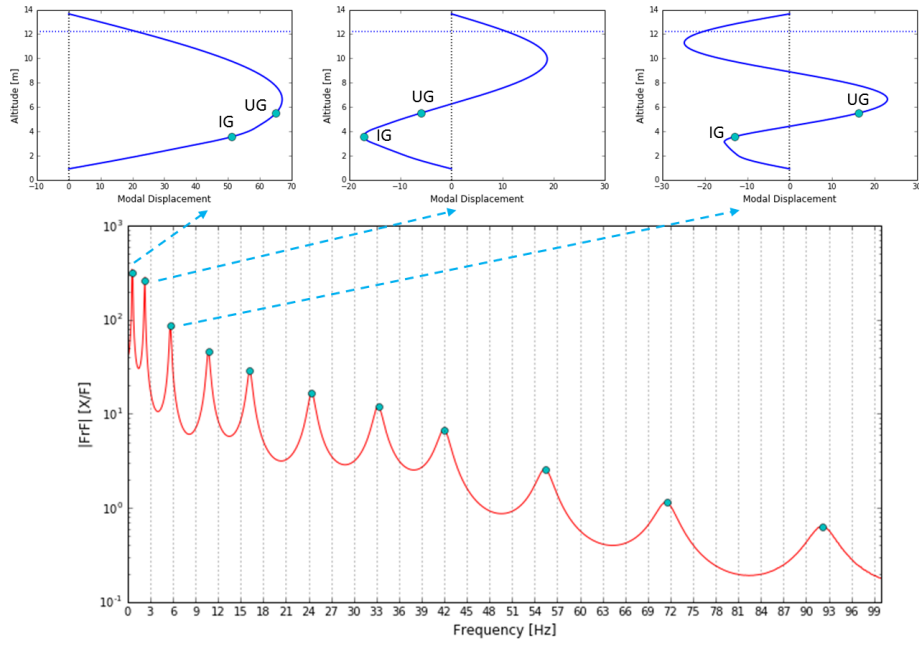


Fig. 3: FRF and first three mode shapes of the MP

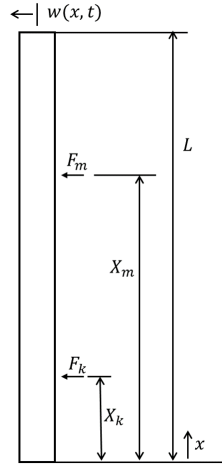


Fig. 4: Simplified MP modeling schematic

DEBSE models the MP as a Euler-Bernoulli beam with sudden geometric changes [13] with N_k number of LS contacts and N_m number of US contacts. The equation of motion for the transverse displacement $w(x, t)$ is:

$$EI(x) \frac{\partial^4 w(x, t)}{\partial x^4} + cI(x) \frac{\partial^5 w(x, t)}{\partial x^4 \partial t} + \rho A(x) \frac{\partial^2 w(x, t)}{\partial t^2} = \sum_{N_k} F_k(t) \delta(x - x_k) + \sum_{N_m} F_m(t) \delta(x - x_m), \quad (1)$$

with c being the Kelvin-Voigt damping coefficient that relates damping to the change in mechanical strain [17], $\rho A(x)$ is the linear mass density, $EI(x)$ is the structural rigidity, and $\delta(x - a)$ is the Dirac-Delta function. In this implementation, the Kelvin-Voigt coefficient is not measured in the physical space, but is assumed to be proportional to the Young's modulus and frequency [13], and is defined via the user selected modal damping coefficients.

For the systems of interest, the boundary conditions (BC) are not simple. Due to the motion of the sleeves, the ends of the MP are subject to enforced displacement and forces. To account for this, a change of variable is introduced [18] and a modal decomposition is applied as:

$$w(x, t) = \phi_0(t)D_0(x) + \phi_L(t)D_L(x) + \sum_N \psi_n(x)q_n(t), \quad (2)$$

where $\phi_0(t)$ and $\phi_L(t)$ are the known displacements at the ends of the MP, $\psi_n(x)$ and $q_n(t)$ are the mode shape and modal time history for mode n , and $D_0(x)$ and $D_L(x)$ are space dependent functions based on the simple BCs (as defined in Table 1). Noting that selecting the origin of the coordinate system can remove either $\phi_0(t)$ or $\phi_L(t)$ from the analysis. The number of modes kept, N , is based on the natural frequencies ω_n . For this work, the natural frequencies and mode shapes depend on simplified BC, such as pin-pin, and some continuity conditions.

Table 1: Derived functions for change of variable shape functions

Boundary Condition	$D_0(x)$	$D_L(x)$
Pin-Pin	$\frac{L-x}{L}$	$\frac{x}{L}$
Pin-Free	$\frac{L-x}{L}$	0
Pin-Clamp	$\frac{x^3}{2L^3} - \frac{3x}{2L} + 1$	$\frac{-x^3}{2L^3} + \frac{3x}{2L}$
Free-Free	0	0
Free-Pin	0	$\frac{x}{L}$
Free-Clamp	0	1
Clamp-Free	1	0
Clamp-Clamp	$\frac{2x^3}{L^3} - \frac{3x^2}{L^2} + 1$	$\frac{-2x^3}{L^3} + \frac{3x^2}{L^2}$
Clamp-Pin	$\frac{x^3}{2L^3} - \frac{3x^2}{L^2} + 1$	$\frac{-x^3}{2L^3} + \frac{3x^2}{2L^2}$

The change of variable in Equation 2 being applied to Equation 1 separates the spacial dependent variables and the time dependent variables. Using the spacial dependent variables calculates the natural frequencies and mode shapes. The resultant equation for the spacial variables becomes:

$$\frac{d^4 \psi_n(x)}{dx^4} = \beta(\omega)^4 \psi_n(x), \quad (3)$$

where β is an undetermined constant that is a function of the applied frequency ω . A general solution to this differential equation gives a form for the mode shapes, such as:

$$\psi_n(x) = a_{n,1} \sin(\beta(\omega)x) + a_{n,2} \sinh(\beta(\omega)x) + a_{n,3} \cos(\beta(\omega)x) + a_{n,4} \cosh(\beta(\omega)x), \quad (4)$$

with $a_{n,\#}$ being an unknown coefficient set to match the BC of the system.

Due to the MSC system geometry, the mode shapes are split into sections corresponding to each section in the geometry [13]. This is represented by a piece-wise function expressed as:

$$\psi_n(x) = \psi_{n,i}(x - x_{0,i}) \text{ if } x \in [x_{0,i}, x_{f,i}], \quad (5)$$

where $x_{0,i}$ and $x_{f,i}$ are the starting and ending locations, and $\psi_{n,i}$ is the mode shape for section i . Similarly to Equation 4, the mode shape for each section takes this generic form with four unique coefficients. To calculate these coefficients, the BC for each section must be known. The first BC, called external BC, are at the extremes of the MP. Table 2 shows these external BC based on the selected BC for an end. For example, "Free-Clamp" would have the two free constraints at the zero end and the clamp constraints at the other end.

The second type of BC is the boundary between each section. Four continuity conditions are used for these transitions (called internal BC). These represent the continuity of the displacement, slope, bending moment, and shear forces across the

Table 2: External boundary conditions

Boundary Condition	Constraint 1	Constraint 2
Pin	$\Psi_n = 0$	$\frac{d^2\Psi_n}{dx^2} = 0$
Clamp	$\Psi_n = 0$	$\frac{d\Psi_n}{dx} = 0$
Free	$\frac{d^2\Psi_n}{dx^2} = 0$	$\frac{d^3\Psi_n}{dx^3} = 0$

section transitions, expressed as:

$$\Psi_{n,i}(L_i) = \Psi_{n,i+1}(0) \quad (6a)$$

$$\frac{d\Psi_{n,i}}{dx}(L_i) = \frac{d\Psi_{n,i+1}}{dx}(0) \quad (6b)$$

$$EI_i \frac{d^2\Psi_{n,i}}{dx^2}(L_i) = EI_{i+1} \frac{d^2\Psi_{n,i+1}}{dx^2}(0) \quad (6c)$$

$$EI_i \frac{d^3\Psi_{n,i}}{dx^3}(L_i) = EI_{i+1} \frac{d^3\Psi_{n,i+1}}{dx^3}(0). \quad (6d)$$

where L_i is the length of section i .

In order to solve for the unknown coefficients, both the external and internal BC are combined into the matrix equation

$$[BC] \{a_i\} = \{0\}. \quad (7)$$

This formulation for the BC matrix has some interesting characteristics. The matrix is dependent on the unknown constant β that is dependent on the applied frequency. One of the main characteristics of this matrix is that when the applied frequency is a natural frequency (ω_n), the matrix is rank deficient [13]. This results in the determinant of the matrix being zero. In order to determine the natural frequencies, a Newton-Raphson algorithm is used on the determinant with the only unknown variable being the applied frequency. Once these frequencies are determined, they are then applied to Equation 7 to get an expression for the mode shapes. Due to the rank deficiency, an arbitrary value is applied for one of the unknown coefficients.

Once the mode shapes are determined, the time dependent variables of Equation 1 can be evaluated. By applying the change of variable and the orthogonality condition of the mode shapes, Equation 1 becomes a set of modal equations of motion expressed as:

$$\frac{d^2q_n(t)}{dt^2} + 2\zeta_n\omega_n \frac{dq_n(t)}{dt} + \omega_n^2 q_n(t) = \sum^{N_k} F_{k,n}(t) - P_n(t) + \sum^{N_m} F_{m,n}(t), \quad (8)$$

where ζ_n is the assigned modal damping, and

$$F_{k,n} = \frac{\Psi_n(x_k)/\rho A(x_k)}{\int_0^L \Psi_n^2(x) dx} F_k(t) = C_{n,k} F_k(t) \quad (9a)$$

$$P_n = \frac{\int_0^L \Psi_n(x) D_0(x) dx}{\int_0^L \Psi_n^2(x) dx} \frac{d^2\phi_0(t)}{dt^2} + \frac{\int_0^L \Psi_n(x) D_L(x) dx}{\int_0^L \Psi_n^2(x) dx} \frac{d^2\phi_L(t)}{dt^2} = D_{n,0} \frac{d^2\phi_0(t)}{dt^2} + D_{n,L} \frac{d^2\phi_L(t)}{dt^2} \quad (9b)$$

$$F_{m,n} = \frac{\Psi_n(x_m)/\rho A(x_m)}{\int_0^L \Psi_n^2(x) dx} F_m(t) = S_{n,m} F_m(t). \quad (9c)$$

For the contact with the US, more consideration is given due to the coupling. Because of this interaction, the US is also modeled as an Euler-Bernoulli beam with a physical equation of motion of:

$$EI_{us}(z) \frac{\partial^4 v(z,t)}{\partial z^4} + cI_{us}(z) \frac{\partial^5 v(z,t)}{\partial z^4 \partial t} + \rho A_{us}(z) \frac{\partial^2 v(z,t)}{\partial t^2} = - \sum^{N_m} F_m(t) \delta(z - z_m), \quad (10)$$

where $v(z, t)$ is the displacement at location z along the beam and the subscript us represent the US material properties. It is important to note that the variables x and z are linearly related and the locations x_m and z_m represent the same physical location. For the US, it is assumed that the BC are free-clamped such that the top of the sleeve is clamped into the ACS. In the analysis, the sleeve motion is calculated simultaneously as the MP through a similar modal decomposition, where $v(z, t) = \sum_{\Gamma} \Psi_{\gamma}(z) Q_{\gamma}(t)$.

2.1 Contact Models

In the derived equations of motion, there are two unknowns: the modal time history and the interaction forces. The contact models used in DEBSE relates these two variables via a functional form. Using this functional form, the equations of motion can be integrated to determine the deflection of the RCS for any time. Currently in DEBSE, there are two contact models programmed. Both models are regulation based, using the relative penetration of the MP and the sleeves. This is calculated as:

$$\Delta_i^b = \left(\frac{p_r + |p_l|}{2} \right)^b - \left(\frac{|p_l| - p_l}{2} \right)^b = \begin{cases} + & \text{Contact on right} \\ - & \text{Contact on left} \\ 0 & \text{No contact} \end{cases}, \quad (11)$$

where i can either be the subscript k for contact with the LS or m for contact with the US, p_r and p_l are the right and left penetration values, and b is an exponent that can take values in the range of [1.0, 1.5]. The formulation of this penetration is designed such that p_r is positive if there is contact on the right side, p_l is negative if there is contact on the left side, and Δ_i^b is the relative penetration [19]. Calculating p_r and p_l depends on if the contact is with the LS or US since one is rigid and the other is elastic. For the rigid LS, these values are calculate as:

$$p_r(t) = \phi_0(t)D_0(x_k) + \phi_L(t)D_L(x_k) + \sum_N \Psi_n(x_k)q_n(t) - \phi_k(t) - (R_{ls}(x_k) - R_{mp}(x_k)) \quad (12a)$$

$$p_l(t) = \phi_0(t)D_0(x_k) + \phi_L(t)D_L(x_k) + \sum_N \Psi_n(x_k)q_n(t) - \phi_k(t) + (R_{ls}(x_k) - R_{mp}(x_k)), \quad (12b)$$

with $\phi_k(t)$ being the known displacement of the LS, $R_{ls}(x_k)$ as the inner radius of the LS, and $R_{mp}(x_k)$ as the outer radius of the MP at the contact location k . For this measurement at a contact location with the US, these equations become:

$$p_r(t) = \phi_0(t)D_0(x_m) + \phi_L(t)D_L(x_m) + \sum_N \Psi_n(x_m)q_n(t) - \sum_{\Gamma} \Psi_{\gamma}(z_m)Q_{\gamma}(t) - (R_{us}(z_m) - R_{mp}(x_m)) \quad (13a)$$

$$p_l(t) = \phi_0(t)D_0(x_m) + \phi_L(t)D_L(x_m) + \sum_N \Psi_n(x_m)q_n(t) - \sum_{\Gamma} \Psi_{\gamma}(z_m)Q_{\gamma}(t) + (R_{us}(z_m) - R_{mp}(x_m)). \quad (13b)$$

These formulations occur for each contact location regardless of the contact model used. Currently, these values are not saved during the integration, but can be recomputed in post-processing.

The first contact model implemented in DEBSE is based on linear springs. In particular, a mass-less, two-stage, linear spring with a gap is applied at each contact location. Since these are linear springs, the penetration coefficient b is set to 1.0 and the force at each contact can be written as:

$$F_i = K_c \Delta_i + \frac{K_m}{2} \begin{cases} (p_r - g_i) + |p_r - g_i| & \text{if } p_r \geq g_i \\ (p_l + g_i) - |p_l + g_i| & \text{if } p_l \leq -g_i \\ 0 & \text{else} \end{cases}, \quad (14)$$

where K_c , K_m , and g_i are user defined quantities. K_c is the first stage stiffness, designed to represent the initial resistance caused by the fluid in the RCS. The second stage represents the material contact in K_m . This is typically orders of magnitude stiffer than the fluid stiffness based on expert knowledge. The transition between stages is measure by the value g_i . While this can be specified for each contact, the current implementation determines this value as a fraction of the undeformed clearance. This is typically around 10% of the clearance, and is characterized by the clearance Adjustment Factor (AF), where $g_i = (1 - AF) * Clearance_i$. The use of this formulation ensures that the second stage of the spring occurs when there is material contact with an adjustable buffer to simulate the fluid effects.

The two-stage spring is able to represent the fluid effect on the dynamics of the MP, but requires a large amount of user knowledge in order to get a realistic result. In order to reduce the required user expertise, a more physical model is

also implemented via the Lankarani and Nikravesh (L&N) contact model [20]. This model looks at the internal collision between two cylinders (similar to a RCS), which forms a nonlinear relationship between the penetration and the contact force, expressed as:

$$F_i = \frac{4}{3} \pi E_i^* \sqrt{R_i^*} L_c \Delta_i^b, \quad (15)$$

where L_c is the user specified length of contact, and:

$$E_i^* = \left(\frac{1 - \nu_{mp}^2(x_i)}{E_{mp}(x_i)} + \frac{1 - \nu_s^2(x_i)}{E_s(x_i)} \right)^{-1} \quad (16a)$$

$$R_i^* = \frac{R_{mp}(x_i) R_s(x_i)}{R_s(x_i) - R_{mp}(x_i)}, \quad (16b)$$

with ν being the Poisson's ratio, and the subscript s referring to either sleeve depending on the location of the contact i (k or m). This model reduces the number of parameters specified by the user. In general the contact length L_c can be based on physical properties of the guide regions and the penetration exponent b has a small range of [1.0, 1.5] with 1.5 representing the contact between two spheres (i.e. circular contact patch compared to the line/elliptical contact expected for a RCS). Some previous work in [15] investigates some of the sensitivity of the simulations to this exponential value. The definition of this model is based the derivation used in [21], which compares various cylindrical contact models. Originally in [20], this contact model only defines the contact pressure and not the equivalent force. If a new implementation is programmed, it is possible to determine the pressure and not require the definition of L_c . In order to show the sensitivity of the contact models, four implementations are used. The first is the spring model with the material stiffness close to the L&N equivalent spring stiffness at the UG for all contact with the US and at the IG for all contacts with the LS. For the other three, the L&N model is used with varied exponent values of $b = \{1.0, 1.25, 1.5\}$.

3 Stepped-Sine Excitation

The first analysis performed to test these various contact models is a single frequency sine excitation in which the frequency is adjusted to determine the dynamic characteristics of the MSC. For this stepped-sine excitation, the frequency is adjusted between 0.2 Hz and 10.0 Hz, with several other aspects remaining constant between simulations. For all the contact models, the modal damping is specified to 2% for all the modes kept, which are all the modes with natural frequencies less than 100 Hz. Additionally for the simulations, a constant time-step of 0.1 ms was used for a duration of six periods of excitation.

There are two main results from these simulations. The first is the time histories of the UG. While showing all the time histories is illogical, they are used to categorize the response and separate the responses into specified regions. The main presented result is the maximum deformation of the UG. To report this, the deformations are normalized by the static estimate for the deformation (around 25 mm) to show the amplification of the dynamic effects. This is called the Dynamic Amplification Factor (DAF). The maximum DAF, along with selected time histories, for these four sweeps is presented in Fig. 5.

In Fig. 5, there are many aspects to note. The first aspect is that the response is categorized into four regions based on the excitation frequency and the response motion at the UG. In order to give a better qualitative understanding of the response, example time histories from each region is also presented in Fig. 5 with the time histories from regions 3&4 having been extended to 12 cycles. Within these time histories, the red dotted line representing the specified IG displacement and the black line representing the calculated UG displacement. Region 1 is comprised of low frequency excitation in which the UG responds at the same frequency of the excitation. For the majority of this section, there is little-to-no variability between the various contact models. This is not the case for very low frequency excitation. The cause of this is believed to be due to the small time step compared to the excitation. A separate test (not shown here) was performed with a larger time step and did not show this variability.

Region 2 is the most diverse and interesting region of this sweep. There are two main characteristics for this region: large amplification and variability caused by numerical issues. This region can also be called the resonance region due to how the response interacts with the natural frequencies of the subsystems. Within this section, there are two natural frequencies that contribute to this varied behavior. The MP has its second natural frequency at 2.3 Hz while the US has its fundamental frequency at 2.1 Hz. Due to the closeness of these frequencies, numerical ill-conditioning becomes a major issue. To better show this variability, Fig. 6 shows a zoomed-in look at this region.

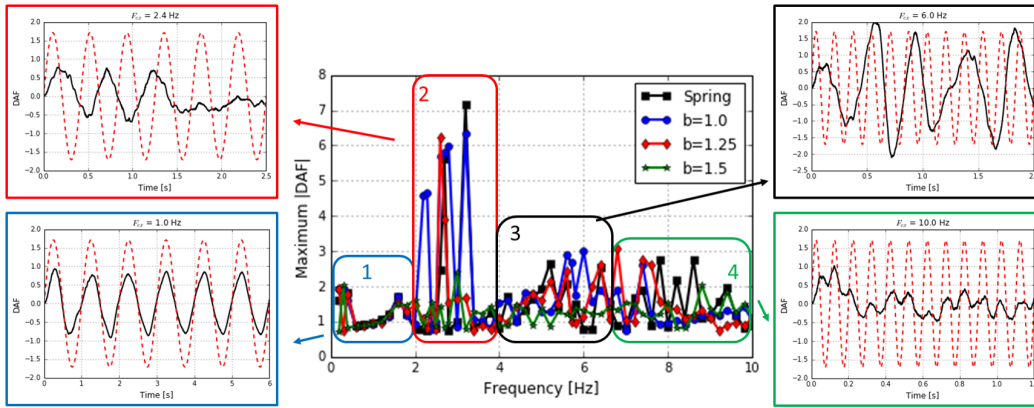


Fig. 5: Maximum normalized deformation from stepped-sine sweep with example time histories.

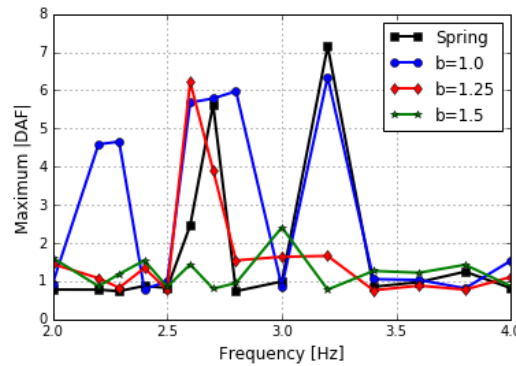


Fig. 6: Focused sweep for the resonance region

The variability in region 2 is due to the ill-conditioning near the combined resonances previously discussed. The main result of this ill-conditioning is the response containing a two-stage response (as noted in the upper left graph in Fig. 5). To better test this hypothesis, a separate simulation was performed with an increased damping coefficient of 5% for the L&N model with the exponent $b = 1.0$. The results from this analysis are presented in Fig. 7. This shows that an increase in damping, which better conditions the equations of motion, eliminates this two-stage response verifying that this is due to the numerical conditioning and not a physical phenomenon. The large increase in the response associated with this region is due to the physical characteristics of the MP's second bending mode (as seen in Fig. 3). For this mode, the IG is near the maximum deformation, signifying that for a small excitation, there is a large response. In this excitation, a large force is being applied at the IG, but the response is bounded by the physical location of the LS thus limiting the amount of energy available for that mode. Since this mode can only exhibit a certain amount of energy, the remaining energy is transferred to the fundamental mode, where the UG has a large displacement.

Regions 3&4 both exhibit large variability between contact models, with the different regions denoted primarily by the time history. Region 3 is dominated by the natural response of the system, while region 4 is a multi-modal response containing both the natural response and the forced response of the system. The variability for both of these regions are large. These frequency ranges exhibit complex responses in which a scalar value (such as the maximum DAF) starts to not fully characterize the response.

The purpose of the pure sine excitation is to characterize the system and better understand its behavior. By looking at the aggregate results across the contact models, a few characteristics can be determined. The first, and most dangerous, is the very large increase in response in the resonant region. This showed a response that is seven times larger than predicted by StaBI. For the physical system, this large deformation would cause contacts with systems that are not currently modeled in the MSC system. In particular, there is a rigid core sleeve that the RCS is placed into to aide in the installation. The clearance between the US and this outer sleeve depends on the core design, but can be slightly larger than the static estimate for this excitation, which is the conservative estimate on the worst-case earthquake scenario. Since the MSC system is not associated with a specified reactor, this actual value is unknown but this aspect is important to keep in mind. The other main characteristic is that the majority of the simulations performed showed maximum DAF larger than 1. There are some areas, in particular in region 3 for certain contact models, that produced a maximum DAF smaller than the static estimate, but the

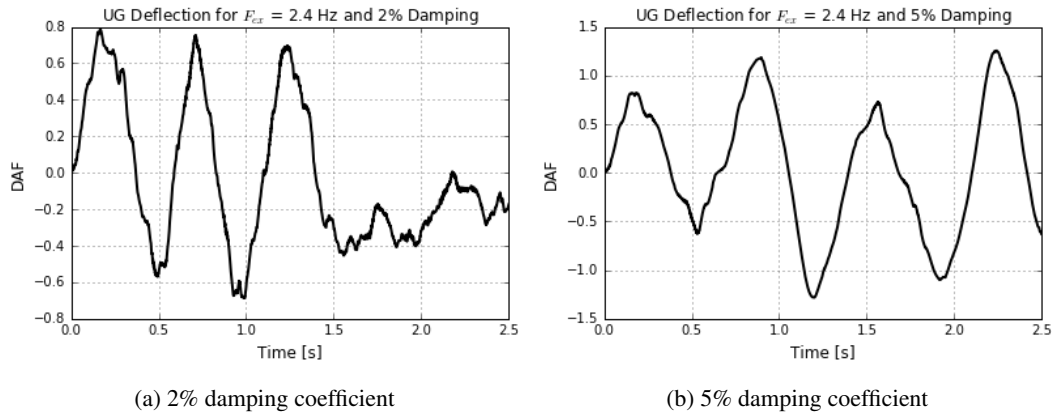


Fig. 7: Effect of increase damping on numerical ill-conditioning

majority of the simulations performed showed an increase due to the dynamic considerations.

4 Static Deformation + Dynamic Excitation

While a pure sine excitation can give insight to how the system reacts, it doesn't show how the system will respond to a real earthquake, which is comprised of several frequencies via a spectrum. Additionally, the displacement used in Section 3 is the accumulation of several possible misalignments. Some of these misalignments are due to static causes (such as installation errors, deformed geometry due to fabrication or bending from irradiation). These account for a displacement on the LS that results in 10 mm at the base and 25 mm at the top of the LS for a conservative estimate. The remaining displacement is comprised of the dynamic excitation caused by the earthquake. To account for the dynamic excitation of the statically deformed RCS, a combination of the tools within PIRAT is used. Specifically, StaBI is used to determine the deformation shape taking into account only the static misalignments, then DEBSE is used to apply a dynamic excitation to this statically deformed system.

For the dynamic excitation, special consideration is used to determine a representative excitation. This is done by using a representative FR core that the MSC could be used in, and the excitation spectrum of the BCS (which the motion of the LS is derived from). The spectrum used is presented in Fig. 8a and consists of 2 dominate frequencies at 0.45 and 4.6 Hz. This spectrum is very similar to the spectrum used for the SPX1 from [9] with different peak frequencies. To convert this spectrum into a time history for the LS, a separate code is used. This code (called BASILIQ^{CAST3M} [22]) takes into account the whole-core system to derive the motion of the LS. The time history produced from this code is shown in Fig. 8b for the excitation at the IG, taking into account the initial deformation. The initial offset of the excitation is based on the static deformation of the LS, while the amplitude is based on a maximum deformation of 5 mm at the base and 20 mm at the top of the LS.

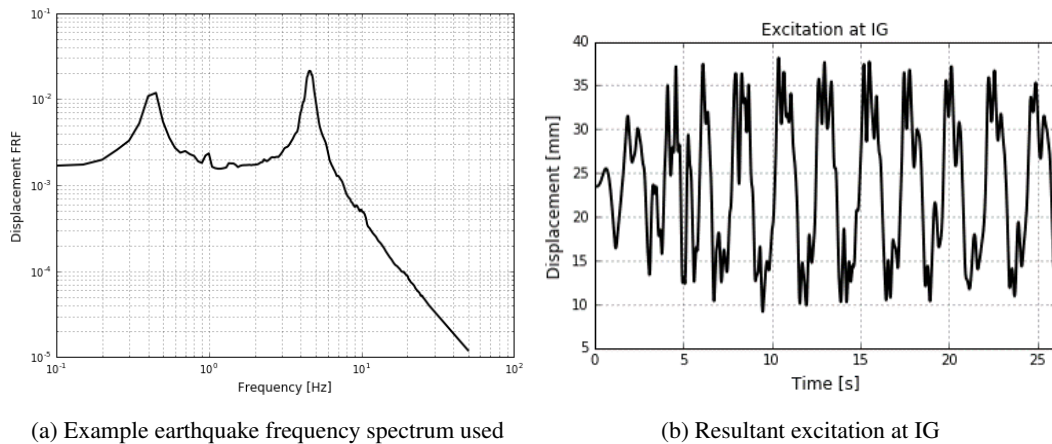


Fig. 8: Dynamic excitation on statically deformed system

A time history like Fig. 8b can be calculated for each point of interest on the LS. With this excitation and the definition of the static deformations, the analysis can be performed. Since StaBI is designed as a black-box, there was not many changes to the run script required to perform this analysis. The main difference was determining the initial modal deformations from the static simulation results. Since the modeled earthquake is severe, the reactor is not expected to be restarted after the earthquake. Due to this, the main interest for the RCS is the first few seconds of dynamic excitation. Once the earthquake is detected the RCS drops the MP into the core to achieve a safe shutdown. This is done on the order of 1 second for FRs [10, 23]. Thus, any large deformations after this shutdown state has occurred is of secondary importance. Currently, DEBSE is only able to calculate fixed height MPs, so while the drop time cannot be calculated, this simulation can give an understanding if the previously used static estimates are reasonable. To show this, the first 10 seconds of the UG response for the dynamic excitation is presented in Fig. 9.

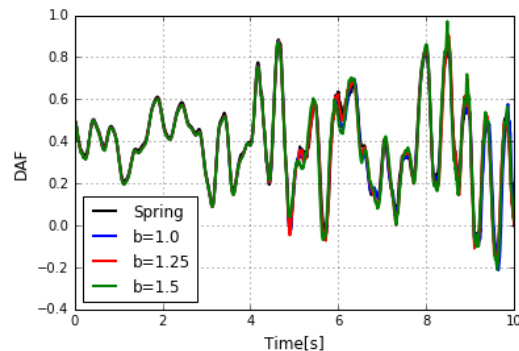


Fig. 9: UG response to dynamic excitation on statically deformed system

The first aspect of Fig. 9 to note are the differences between the contact models. There are very little differences between these models, with the only differences appearing as the magnitude at the peaks. This highly suggests that for realistic simulations, the choice of contact model does not greatly affect the results of the simulation. This brings confidence to the simulations used since the main aspect decided by the user does not greatly affect the results. Another main aspects of the results are associated with the physical significance of the results. In Fig. 9, there are times where the deflection of the UG is negative while the IG is always positive (see Fig. 8b). This can create a large shear force on the MP that opposes the dropping motion. One caveat is that this does not occur until 5 seconds into the simulation, where it is expected that the full drop would have occurred. Even if it has not, this instance is only for a short amount of time that could initiate a stick-slip condition of the drop, where the MP stops moving for a very short duration of time. This starts to become a greater issue later on in time since the amount of time that this out-of-phase deformation is occurring increases.

The last main aspect of the results is associated with the maximum deformation. In Fig. 9, the maximum deformation for the entire simulated time is calculated using the L&N contact model with $b = 1.5$ that produces a maximum DAF of slightly below 1 (0.97). This suggests that the quasi-static simulation could be conservative, which can be used to give a conservative drop time using the SIKI tool. The idea of conservatism is based on more factors than just the maximum deformation (i.e. friction/contact forces, fluid interactions, etc.), but these results give some evidence that the static estimates might be conservative.

5 Conclusions

This work shows the dynamic modeling of a Reactivity Control System using the newly developed toolbox PIRAT. In particular, focus was put on the dynamic solver DEBSE and how that solver models the interaction between multiple subsystems. This work takes two implemented models (a mass-less, two-stage, linear spring and the Lankarani & Nikravesh contact model) and compares the variability between these models to commonly used excitations. The first excitation is a single-frequency sine excitation that is stepped through various frequencies, leading to several findings:

- * By investigating the time histories, 4 distinct types of responses are found that depend on the frequency of excitation.
- * Low frequency excitation showed very little variation between contact models while higher frequency excitation showed a large variability.
- * One region was found to produce large deformations (around 7 times the static estimation) that is caused by the resonant effects of the system. This region also had a large variability due to numerical ill-conditioning that was caused by the resonance coupling of the subsystems.

- * Due to these findings, actual excitations must be checked against the possibility of exciting the system with a large fraction of the excitation energy occurring near a resonance frequency [15].

The other excitation is a realistic expression of the deformation that this type of system would experience during a severe earthquake. This includes the idea of separating the deformation into static and dynamic components. The static components of the deformation (caused by installation/fabrication uncertainty and irradiation bending for example) comprise of approximately half of the expected deformation of the system. For the dynamic excitation, the time history is calculated by the BASILIQ code based on a representative reactor core that the MSC system could be used in. This separation of deformations uses multiple solvers in PIRAT, where StaBI is used to calculate the deformation due to the static deformations and DEBSE is used to calculate the dynamic response to the earthquake on the statically deformed system. The results from these simulations produces several interesting findings:

- * With a focus on the short time frame (0 – 10 seconds of excitation), there was very little variation between the contact models. While this was not found for the pure sine excitation, this gives confidence in the simulations to produce realistic responses for the most challenging aspect in designing a Reactivity Control System.
- * In addition to the variability, the results also show some interesting aspects for the analysis in general. During the simulation time, there was no displacement greater than the quasi-static estimate, giving evidence that the static analysis might be sufficient to calculate the drop time.

References

- [1] Brochard, D., and Buland, P., 1987. “Seismic qualification of SPX1 shutdown systems - tests and calculations”. In Proceedings of the ICONE-11 Conference.
- [2] Martelli, A., Forni, M., Masoni, P., Maresca, G., Castoldi, A., and Muzzi, F., 1988. “Research and development studies on plant and core seismic behaviour for a fast reactor”. *Nuclear engineering and design*, **106**(1), pp. 103–126.
- [3] Zabiégo, M., Lorenzo, D., Helfer, T., and Guillemin, E., 2017. “Insertion reliability studies for the RBC-type control rods in ASTRID”. In Proceedings of FR17 Conference. Paper IAEA-NC-254-120.
- [4] Chellapandi, P., Babu, V. R., Chetal, S., and Baldev, R., 2006. “Performance evaluation of control and safety rod and its drive mechanism of fast breeder reactor during seismic event”. In 14th International Conference on Nuclear Engineering, American Society of Mechanical Engineers, pp. 109–117.
- [5] Babu, V. R., Veerasamy, R., Patri, S., Raj, S. I. S., Krovvidi, S. K., Dash, S., Meikandamurthy, C., Rajan, K., Puthiyavinayagam, P., Chellapandi, P., Vaidyanathan, G., and Chetal, S., 2010. “Testing and qualification of control & safety rod and its drive mechanism of fast breeder reactor”. *Nuclear Engineering and Design*, **240**(7), pp. 1728 – 1738.
- [6] Morrone, A., Nahavandi, A., and Brussalis, W., 1976. “Scram and nonlinear reactor system seismic analysis for a liquid metal fast reactor”. *Nuclear Engineering and Design*, **38**(3), pp. 555 – 566.
- [7] Sundaran, M., Vijayashree, R., Raghupathy, S., and Puthiyavinayagam, P., 2017. “Experimental seismic qualification of diverse safety rod and its drive mechanism of prototype fast breeder reactor”. In Proceedings of the FR17 Conference. paper IAEA-CN-254-344.
- [8] Nakagawa, M., and Jodoi, T., 1991. “Insertion analyses of articulated control rods under seismic excitation”. In Transactions of the 11th international conference on structural mechanics in reactor technology.
- [9] Gantenbein, F., Gauvain, J., Bernard, A., and van Dorsselaere, J., 1983. “Seismic behavior of a fast reactor core. application on superphenix 1”. *Proceedings of the SMiRT7 Conference*, August, pp. 299–306.
- [10] Son, J. G., Lee, J. H., Kim, H. W., Kim, S. K., and Kim, J. B., 2019. “Influence of design modification of control rod assembly for prototype generation IV sodium-cooled fast reactor on drop performance”. *Nuclear Engineering and Technology*, **51**(3), pp. 922–929.
- [11] Courbon, J., 1980. “Théorie des poutres”. *Techniques de l'ingénieur*(C2010). (In French).
- [12] Bonney, M., and Zabiégo, M., 2018. “Validation of PIRAT, a novel tool for beam-like structures subject to seismic induced misalignment of guiding sleeves”. In Proceedings of the 2018 International Conference on Noise and Vibration Engineering. Paper #172.
- [13] Koplow, M., Bhattacharyya, A., and Mann, B., 2006. “Closed form solutions for the dynamic response of Euler - Bernoulli beams with step changes in cross section”. *Journal of Sound and Vibration*, **295**(1), pp. 214 – 225.
- [14] Bonney, M., and Zabiégo, M., 2019. “PIRAT - an analytical tool for insertion reliability assessment of reactivity control systems - progress and applications to sodium fast reactors”. *Proceedings of the 2019 International Congress on Advances in Nuclear Power Plants*, May.
- [15] Bonney, M., and Zabiégo, M., Submitted. “Dynamic modeling of reactivity control systems for scram reliability assessment in fast reactors under seismic conditions”. *Nuclear Engineering and Design*.
- [16] Arnaud, G., Guigon, A., and Verset, L., 1984. “Les barres de commande des RNR français expérience et développement”. In Proceedings of the IAEA International Working Group on Fast Reactors specialists meeting on absorber materials and control rods for fast breeder reactors, pp. 29–38.

- [17] Liu, K., and Liu, Z., 1998. “Exponential decay of energy of the Euler–Bernoulli beam with locally distributed Kelvin–Voigt damping”. *SIAM journal on control and optimization*, **36**(3), pp. 1086–1098.
- [18] Gou, P., and Panahi, K., 2001. “Analytical solution for beam with time-dependent boundary conditions versus response spectrum”. In Proceedings of the 9th International Conference on Nuclear Engineering.
- [19] Praveen Krishna, I. R., and Padmanabhan, C., 2012. “Experimental and numerical investigations of impacting cantilever beams part 1: first mode response”. *Nonlinear Dynamics*, **67**(3), Feb, pp. 1985–2000.
- [20] Lankarani, H. M., and Nikravesh, P. E., 1994. “Continuous contact force models for impact analysis in multibody systems”. *Nonlinear Dynamics*, **5**(2), pp. 193–207.
- [21] Pereira, C. M., Ramalho, A. L., and Ambrósio, J. A., 2011. “A critical overview of internal and external cylinder contact force models”. *Nonlinear Dynamics*, **63**(4), pp. 681–697.
- [22] Broc, D., Cardolaccia, J., and Martin, L., 2014. “Physical and numerical methods for the dynamic behavior of the fast reactor cores”. In ASME 2014 Pressure Vessels and Piping Conference, American Society of Mechanical Engineers.
- [23] Lee, Y., Lee, J., Kim, H., Kim, S., and Kim, J., 2017. “Drop performance test of conceptually designed control rod assembly for prototype generation IV sodium-cooled fast reactor”. *Nuclear Engineering and Technology*, **49**(4), pp. 855–864.